Comparison of poloidal velocity measurements to neoclassical theory on the National Spherical Torus Experiment[a)]

R. E. Bell,[1,b)] R. Andre,[1] S. M. Kaye,[1] R. A. Kolesnikov,[1,c)] B. P. LeBlanc,[1] G. Rewoldt,[1] W. X. Wang,[1] and S. A. Sabbagh[2]
[1]*Princeton Plasma Physics Laboratory, Princeton University, Princeton, New Jersey 08543, USA*
[2]*Department of Applied Physics and Applied Mathematics, Columbia University, New York, New York 10027, USA*

(Received 8 April 2010; accepted 22 July 2010; published online 20 August 2010)

Knowledge of poloidal velocity is necessary for the determination of the radial electric field, which along with its gradient is linked to turbulence suppression and transport barrier formation. Recent measurements of poloidal flow on conventional tokamaks have been reported to be an order of magnitude larger than expected from neoclassical theory. In contrast, poloidal velocity measurements on the NSTX spherical torus [Kaye *et al.*, Phys. Plasmas **8**, 1977 (2001)] are near or below neoclassical estimates. A novel charge exchange recombination spectroscopy diagnostic is used, which features active and passive sets of up/down symmetric views to produce line-integrated poloidal velocity measurements that do not need atomic physics corrections. Inversions are used to extract local profiles from line-integrated active and background measurements. Poloidal velocity measurements are compared with neoclassical values computed with the codes NCLASS [Houlberg *et al.*, Phys. Plasmas **4**, 3230 (1997)] and GTC-NEO [Wang *et al.*, Phys. Plasmas **13**, 082501 (2006)].
 [doi:10.1063/1.3478571]

I. INTRODUCTION

The radial electric field (E_r) and its gradient have been linked to turbulence suppression and transport barrier formation in tokamak plasmas. Accurate measurements of E_r are also required for evaluating the pitch angle of the magnetic field when using the motional Stark effect (MSE).[1] E_r is typically determined by evaluating the individual terms of the radial force balance equation

$$E_r = \frac{\nabla p}{eZn} + v_\phi B_\theta - v_\theta B_\phi, \tag{1}$$

where the ion pressure p, ion density n, toroidal velocity v_ϕ, and poloidal velocity v_θ, are determined for any single ion species with charge eZ, and B_ϕ and B_θ are the toroidal and poloidal components of the magnetic field, respectively. The most commonly used tool to evaluate these terms is charge exchange recombination spectroscopy using impurity ions. High energy heating beams can penetrate to the plasma core and charge exchange (CX) with impurity ions that would otherwise be fully ionized, making spectroscopic measurements possible. Localized measurements of toroidal velocity, ion temperature, and ion density for impurity ions are routinely made on many tokamaks. Measurements of poloidal velocity are far more challenging due to much smaller velocities and more complicated atomic physics issues, so a neoclassical calculation is often relied upon to evaluate the poloidal velocity term for the determination of E_r.

Some recent measurements of poloidal velocity differ by an order of magnitude with neoclassical predictions: on JET in the region of an internal transport barrier (ITB),[2,3] and on DIII-D during *H*-mode and quiescent *H*-mode discharges,[4] where the direction of the poloidal flow also differed from the neoclassical expectation. Measurements of poloidal flow on JT-60U plasmas with an ITB, however, were found to be consistent with neoclassical theory within experimental error.[5] Poloidal velocity measurements on the low aspect ratio spherical tokamak MAST were also found to be consistent with neoclassical theory within experimental error for *L*- and *H*-mode plasmas.[6] In all of these cases, substantial atomic physics corrections to the apparent velocity were required to obtain the inferred poloidal velocity.

A new poloidal-viewing diagnostic on the National Spherical Torus Experiment[7] (NSTX) has been designed with an optimized viewing geometry to take advantage of plasma symmetry to avoid many of the atomic physics complications of poloidal velocity measurements using CX recombination spectroscopy. When comparing experiment to neoclassical theory, it is advantageous to make poloidal flow measurements on a spherical tokamak operating with inherently low magnetic field and with modest ion temperature, since a dominant atomic physics effect, namely the gyro orbit finite-lifetime effect,[8] which scales with ion temperature and magnetic field, is strongly suppressed. While symmetric views from above and below the midplane screen out non-poloidal velocity components due to atomic physics effects, views both through and away from the neutral beams isolate the CX emission in the beam volume. Line-integrated measurements from the dedicated background views away from the neutral beam are inverted to obtain local background emission profiles, which is interpolated to the active viewing

[a)]Based on an invited talk presented at the APS DPP Meeting in Atlanta in November 2009. Paper NI3 3, Bull. Am. Phys. Soc. **54**, 181 (2009).
[b)]Invited speaker. Electronic mail: rbell@pppl.gov.
[c)]Present Address: Los Alamos National Laboratory, Los Alamos, NM 87545.

locations. The line-integrated background profile contribution is then computed for the active view and subtracted from the active view measurements. Due to the finite height of the neutral beam, the charge exchange brightness and apparent velocity after background subtraction are also inverted to obtain local poloidal velocity profiles.

Two distinct simulation codes are used to compute neoclassical poloidal velocity for comparison with measurements: NCLASS (Ref. 9) and GTC-NEO.[10] The code NCLASS calculates neoclassical-transport properties of a multispecies axisymmetric plasma of arbitrary aspect ratio, geometry, and collisionality. Measured plasma profiles are input to NCLASS from TRANSP,[11] a tokamak transport analysis code. NCLASS can be run as a module in TRANSP or externally. The GTC-NEO code has been recently modified to handle impurity species, allowing the simulation of the carbon poloidal velocity.[12] The GTC-NEO code includes finite-orbit-width (banana width) effects and calculated fluxes are nonlocal relative to the driving density and temperature gradients with additional smoothing over the banana width scale. The NCLASS code, on the other hand, does not include finite-orbit-width effects and self-consistent neoclassical electric field, and the transport fluxes at any radius depend only on the gradients at that radius. In this sense, NCLASS is less complete and accurate than GTC-NEO, particularly when nonlocal effects are important. One major effect which makes GTC-NEO results less accurate near the edge is realistic boundary conditions such as particle loss which may play an important role in determining edge neoclassical transport and has not been taken into account in current GTC-NEO simulation. The GTC-NEO code uses the same measured plasma profiles and equilibrium from TRANSP as NCLASS, and a magnetohydrodynamics equilibrium recomputed from TRANSP data.

New poloidal velocity measurements from NSTX are found to be near or below neoclassical estimates in magnitude and are consistent in direction. Poloidal velocity profiles for H-mode plasmas are compared, while systematically changing the direction and magnitude of the toroidal magnetic field. This paper is organized as follows. The issues relating to the measurement of poloidal flow using CX recombination spectroscopy are presented in Sec. II. The diagnostic approach used to measure poloidal velocity on NSTX is described in Sec. III. The inversion method to obtain local velocities from line-integrated measurements is detailed in Sec. IV. Line-integrated poloidal velocity measurements are presented in Sec. V. Comparison of measured velocity profiles to neoclassical theory are presented in Sec. VI.

II. ISSUES WITH POLOIDAL VELOCITY MEASUREMENTS

A. Practical issues

There can be a very large difference in the magnitude of poloidal and toroidal velocities. While toroidal velocities can be hundreds of km/s, poloidal velocities are expected to be a few km/s. Differentiating small poloidal velocities from much larger toroidal velocities requires that poloidal viewing sightlines must be known to a few arcminutes of angle. Even when measuring in a radial plane, the alignment of views must be such that the toroidal contribution is small compared to the fitting error.

The small poloidal velocity values can be subject to small but significant systematic errors. The wavelength shift associated with a velocity of 1 km/s is 0.0176 Å at 5290 Å. A systematic change in wavelength on this scale can occur with changes in the index of refraction of air due to changes in air pressure or temperature. These changes in refractive index can be quantified using the Ciddor equation.[13] For instance, a change in barometric pressure of 2%, which might be experienced with a weather front, would result in an apparent wavelength change of 0.013 Å equivalent to a change in velocity of 0.74 km/s. Systematic shifts in measured velocity can occur if the barometric pressure changed between the time of the wavelength calibration and the time of the rotation measurements. Changes in temperature could also be an issue if the spectrometer is not kept in a climate-controlled environment.

The rest wavelength of the $n=8-7$ C VI transition used here is nominally 5290.53 Å in air,[14] but the exact value is dependent on the ion temperature, shifting lower in wavelength for lower temperature.[15] Assuming a statistical population of states, a change in central wavelength of 0.054 Å is calculated for C VI when the temperature changes from 100 eV to 3 keV (the range of NSTX thermal ion temperatures) corresponding to an apparent velocity shift of 3 km/s. Systematic shifts of this magnitude are significant for poloidal flow measurements, though less critical for the typically larger toroidal flow measurements.

B. Energy dependent CX cross section

CX recombination spectroscopy takes advantage of an electron capture by an impurity ion from a beam neutral

$$D^0(n_D) + C^{6+} \rightarrow D^+ + C^{5+}(n), \tag{2}$$

where the deuterium beam neutral is usually in the ground state ($n_D=1$), with a tiny fraction in an excited state ($n_D>1$). The product impurity ion with a single electron is in an excited state (n). The levels most likely to be populated are $n \approx n_D Z^{3/4}$,[16,17] where Z is the charge of the impurity ion. On NSTX, for the $n=8-7$ transition of C^{5+}, the CX with beam neutrals in the ground state will preferentially populate the $n=4$ level. Excited beam neutrals in the $n_D=2$ state will preferentially populate the $n=8$ level, the upper level of the observed transition. The excited product ion will emit a photon promptly ($\approx 10^{-9}$ s for $n=8$ C^{5+}) providing a localized measurement before rapidly decaying into the ground state.

The local CX emission is proportional to the beam neutral density, the carbon impurity density, and the CX rate

$$E^{\mathrm{CX}} = n_{\mathrm{beam}} n_{C^{6+}} \langle \sigma v \rangle^{\mathrm{CX}} \tag{3}$$

with

$$\langle \sigma \nu \rangle^{\mathrm{CX}} = \int\int\int \sigma^{\mathrm{CX}} |\vec{v} - \vec{v}_{\mathrm{beam}}| f(\vec{v} - \vec{v}_{\mathrm{rot}}) dv^3, \tag{4}$$

where $\sigma^{\mathrm{CX}} = \sigma^{\mathrm{CX}}(|\vec{v} - \vec{v}_{\mathrm{beam}}|)$ is the CX cross section which depends on the collision velocity between the carbon impu-

rity and the beam neutral, $f(\vec{v})$ is the Maxwellian velocity distribution of the C^{6+} ions, and $\vec{v}_{\rm rot}$ is the rotational velocity of the C^{6+} ions. The CX cross section depends strongly on the collision energy for the range of energies typically used on neutral beams, peaking around 60 keV/amu and decreasing rapidly toward lower collision energies where neutral beams will interact. With deuterium neutral beams, there are full, half, and third energy components due to the molecular makeup of the deuterium in the beam source. Each of these beam components will sample a different portion of the energy dependent cross section. On NSTX, a typical deuterium beam voltage of 90 kV will result in collision energies near 45, 22, and 15 keV/amu. The cross section of an excited beam neutral with $n_D=2$, which peaks around 6 keV/amu, is two orders of magnitude greater than for the ground state. The excited neutrals can greatly alter the effective cross section for low collision energies even with a tiny fraction (a few tenths of a percent) in that state.

The main effect of the energy dependent cross section is to introduce an apparent velocity shift that is not associated with the parent C^{6+} ion distribution. A Maxwellian distribution of C^{6+} ions interacting with a monodirectional neutral beam will have higher collision energies for ions moving toward the beam and lower collision energies for ions moving away from the beam. The C^{5+} ion production will be enhanced for the part of the distribution moving toward the beam and suppressed for the part moving away from the beam. This will give rise to a net flow of C^{5+} ions toward the neutral beam. This is a *real velocity* (of the product C^{5+} ions) that will be additive to the flow of the C^{6+} parent distribution. This net flow velocity toward the beam will scale up with ion temperature, since a wider range of the gradient of the CX cross section is sampled at higher temperature.

The inherent uncertainties of the computed CX rates must be considered when dealing with the small values of poloidal velocity. Estimated uncertainties in electron capture cross sections for ground state neutrals with C^{6+} $n=8$ ions are 50% or larger for collision energies below 20 keV/amu.[17] This is the range where half and third energy deuterium neutrals contribute to the measured spectrum. Apparent shifts in wavelength depend on the shape of these CX cross sections at collision energies where the uncertainties are large. Uncertainties in the effective emission rates, which are based on the electron capture cross sections, may result in significant uncertainty in measured velocity compared to the actual poloidal velocity.

While the velocity distribution of the parent ion (C^{6+}) is the desired quantity, the velocity of the product ion (C^{5+}) emission is actually measured. The measured line-integrated signal also includes other emission from C^{5+}, including intrinsic emission that exists near the plasma edge. It is also possible for the product ion to be re-excited by electron impact and emit again before ionization ($\approx 10^{-4}$ s) producing "plume" emission.[18] This is nonlocal emission, since the plume ions have time to drift away from their birth location in the beam volume due to parallel ion flow. Depending on the viewing geometry, plume emission originating near the edge could be viewed in sightlines that view the plasma center. Since CX emission is weaker in the core due to attenuation of the beam, the effect of plume emission would have a greater effect on apparent ion temperature and velocity there. Plume emission due to carbon is readily observable on NSTX,[19] and it makes up about half of the background emission when observing the plasma center on both the toroidal and poloidal views. On many tokamaks, beam modulation is used to separate the desired CX emission from the intrinsic emission, but beam modulation cannot remove unwanted emission from plume ions.

C. Gyro orbit finite lifetime effects

When measuring in the plane of the gyro orbit, the motion of an ion and the lifetime of the excited state become important.[8] If there is a component of the neutral beam velocity in the plane of the gyro orbit, the collision energy will vary around the gyro orbit. If the product ion does not emit immediately, some of the net flow toward the beam will be redirected vertically. If the effective lifetime of the upper n level of the observed transition is τ, then the ion will rotate $\omega\tau$ before radiating, where ω is the ion gyrofrequency. This will result in an apparent velocity directed vertically that will scale with the magnetic field (due to ω) and with ion temperature (due to net flow from the energy dependent cross section). The value of τ has been measured to be about 1 ns;[8] the lifetime depends on the electron density and the relative populations of the fine structure components of the $n=8$ level. The gyro orbit finite-lifetime effects were quite large on TFTR; for 30 keV ions with $B=5$ T, $\omega\tau=0.25$ rad, the vertical velocity was ≈ 40 km/s, dominating the poloidal flow. On NSTX, the ion temperature and magnetic field are each lower by an order of magnitude or more, so this velocity is a few 100 m/s or less, smaller than the experimental error in the measured velocity.

III. DIAGNOSTICS

The issues outlined in Sec. II motivated the design of the poloidal-viewing CX spectroscopy system on NSTX, which is similar to the system used on TFTR.[20] High throughput optics and high quantum efficiency detectors are used to increase the signal to noise ratio so that the fitting error is less than 1 km/s. Active and passive views are used to separate the CX emission from intrinsic background and plume emission. The active views refer to sightlines viewing across the neutral beams, which includes both CX emission and background emission. The passive views refer to sightlines at a toroidal location away from the neutral beams, which measure only background emission. The NSTX neutral beams are aimed horizontally. Recognizing that the effects of the energy dependent CX cross section will result in a horizontal flow toward the neutral beam, the up/down symmetry of the plasma and the beam geometry with respect to the midplane were exploited to avoid complex corrections for the atomic physics issues that would be necessary for a single viewing direction. The use of up/down symmetric views virtually eliminates the typical reliance on computation of beam attenuation, CX cross sections, beam neutral excitation, and relative fraction of the beam energy components when determining the *line-integrated* poloidal velocity.

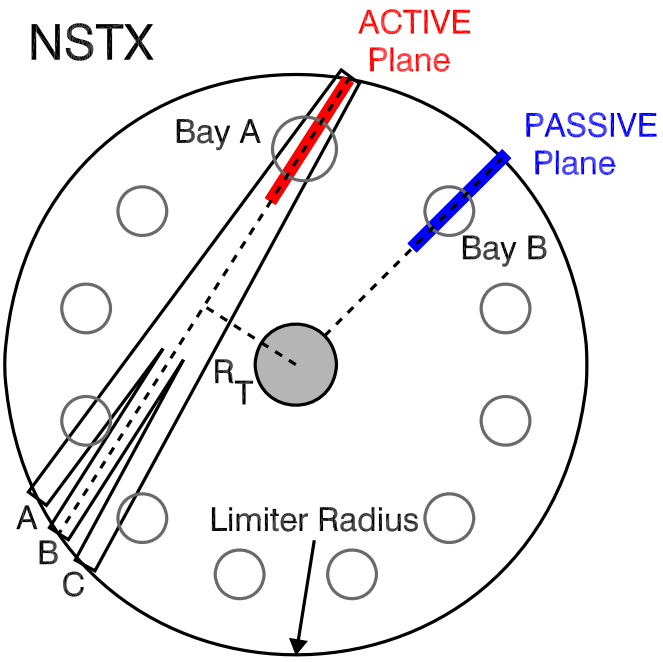

FIG. 1. (Color online) Plan view of NSTX midplane showing the locations of the active and passive detection planes. The active plane has the same tangency radius R_T as the central of three neutral beam sources labeled A, B, and C.

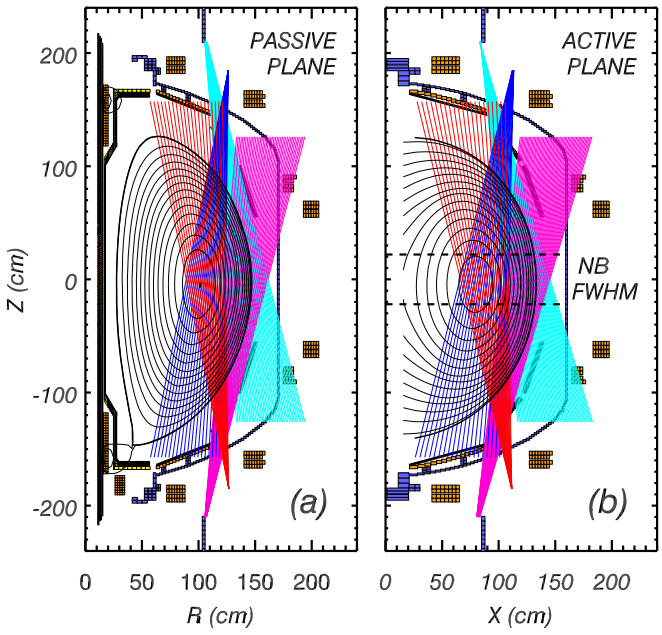

FIG. 2. (Color online) Cross section of NSTX showing poloidal viewing sightlines in (a) passive plane and (b) active plane. Each upward and downward viewing pair of sightlines is precisely aligned at the midplane. There are 63 pairs of sightlines in the passive view and 75 pairs of sightlines in the active view.

A. Up/down symmetric viewing geometry

Special port locations above and below the neutral beam were included in the design of the NSTX vacuum vessel to accommodate a poloidal velocity measurement. Figure 1 shows the locations of the detection planes. The active detection plane is aligned with the central of three tangential neutral beam sources. The passive plane is purely radial and toroidally separated from the neutral beams to view only background emission. Figure 2 shows the upward and downward viewing sightlines in the active and passive planes. The viewing planes view the plasma through gaps in the passive plates. These sightlines either terminate in these gaps, which act as effective light dumps, or terminate at near normal incidence on carbon tiles, so reflections are not an issue. The horizontal coordinate for the passive viewing plane is major radius (R); the horizontal coordinate for the active views is $X=\sqrt{R^2-R_T^2}$, where R_T is the tangency radius of the detection plane. The active plane is tangential, so nonvertical sightlines will have a small toroidal component contributing to the apparent velocity. Eight lenses at four locations are used to collect light for 276 optical fibers, giving 75 pairs of active viewing fibers and 63 pairs of passive viewing fibers. The radial resolution after inversion is $\Delta r=0.6$ cm in the outer region and $\Delta r \leq 1.8$ cm near the plasma center. With the low magnetic field on NSTX, the edge spatial resolution is comparable to the ion gyroradius.

Precise measurements of the sightlines were made by back illuminating the optical fibers and using an articulated measuring arm to fit an ellipse to each fiber image in several vertical-spaced planes. The optical path of each fiber was then fitted in three dimensions and the virtual point, from which all these optical paths emanated, was determined using a least squared regression. This process was repeated for each lens system in the collection optics. The viewing angle of each sightline is known to better than 0.01°. Precise alignment of the viewing chords at the midplane allows matching of upward and downward views to better than 1 mm.

Up/down symmetric views are used to subtract horizontal components of the velocity due to toroidal flow or the flow toward the neutral beam induced by the energy dependent CX cross section. The apparent product ion velocity of the plasma, $\vec{v}$, can be described as the sum of the poloidal and toroidal components of the flow as well as the contributions of the velocities induced by the energy dependent CX cross section

$$\vec{v}=\vec{v}_\theta+\vec{v}_\phi+\vec{v}_{cx}+\vec{v}_{gfl}, \tag{5}$$

where $\vec{v}_{cx}$ refers to the net velocity of the product ion towards the beam and $\vec{v}_{gfl}$ refers to the resultant flow due to the gyromotion finite lifetime effect. The apparent velocity along a particular sightline is given by

$$v_{\rm app}^{\pm}=\hat{s}^{\pm}\cdot\vec{v}=\pm\beta_1 v_\theta+\alpha_1 v_\phi+\alpha_2 v_{cx}\pm\beta_2\omega\tau v_{cx}, \tag{6}$$

where

$$\hat{s}^{\pm}=s_x\hat{x}+s_y\hat{y}\mp s_z\hat{z} \tag{7}$$

refers to unit vectors for upper (+) and lower (−) sightline directions. The coefficients for quantities which do not depend on viewing direction are $\alpha_1=|\hat{s}\cdot\hat{\phi}|$, $\alpha_2=|\hat{s}\cdot\hat{n}|$, where $\hat{n}$ is a unit vector directed along the neutral beam velocity. The coefficients for quantities that depend on viewing direction are $\beta_1=|\hat{s}\cdot\hat{v}|$ and $\beta_2=|\hat{s}\cdot\vec{B}\times\hat{n}|/B$, where $\hat{v}$ is a unit vector in the direction of the poloidal velocity. A differential velocity

is obtained by taking half the difference of the apparent velocities from the upper and lower views

$$v_{\mathrm{diff}} = \tfrac{1}{2}(\vec{v}^{+}_{\mathrm{app}} - \vec{v}^{-}_{\mathrm{app}}) = \beta_1 v_\theta + \beta_2' \omega\tau v_{cx} \approx \beta_1 v_\theta, \tag{8}$$

where $\beta_2' = |\hat{s}\cdot\vec{B}_\phi \times \hat{n}|/B$, using only the toroidal part of the magnetic field, since the associated horizontal terms cancel. Since $\omega\tau$ is small compared to the fitting error, the differential velocity depends only on the desired poloidal velocity and the viewing direction. The actual measurements are line-integrated so the line-integrated differential velocity relies on the up/down symmetry of the plasma for the cancellation of the horizontal components due to v_ϕ and v_{cx} along the sightlines

$$u_{\mathrm{diff}} = \frac{1}{2}\left(\frac{\int E^{\mathrm{CX}} v^{+}_{\mathrm{app}} d\ell}{\int E^{\mathrm{CX}} d\ell} - \frac{\int E^{\mathrm{CX}} v^{-}_{\mathrm{app}} d\ell}{\int E^{\mathrm{CX}} d\ell}\right), \tag{9}$$

where u_{diff} is the differential line-integrated velocity. In this work, the variable u is used for line-integrated velocities and the variable v is used for local velocities.

Differential velocity measurements eliminate the need to precisely know the rest wavelength of the transition. Small systematic errors due to drifts in wavelength calibrations will also cancel. Line-integrated differential velocity measurements do not need atomic physics corrections, since horizontal contributions cancel and the contribution due to the gyro orbit finite lifetime effects are negligible with the low magnetic field on NSTX.

B. Supporting diagnostics and systems

The three neutral heating beam sources on NSTX, which are used for CX spectroscopy, are all located at one toroidal location (see Fig. 1). Each source is nominally 12 cm wide and 42 cm tall. The sources intersect near the plasma edge and have an angular separation of about 4°.

Two midplane diagnostics are used to support the poloidal velocity measurement on NSTX. A multipoint Thomson scattering (MPTS) diagnostic provides T_e and n_e profiles at 60 Hz. A midplane toroidal CX recombination spectroscopy (CHERS) diagnostics is used to provide local ion temperature (T_i), carbon density (n_C), and v_ϕ profiles at 100 Hz. The toroidal CHERS system also uses active and passive views to allow the simultaneous subtraction of background emission from the active view. The toroidal CHERS system has a radial resolution $\Delta r = 0.6-3$ cm (edge to core) for the active view across the neutral beams. The background view runs parallel to the neutral beams. Since all neutral beams are at the same toroidal location, beam modulation is not a practical method to suppress background contributions to the measured signal on NSTX, since it would require a 100% modulation of the beam power. Separate passive views require more total sightlines and a more demanding calibration sequence, but they do provide a simultaneous removal of both intrinsic and plume emission from CX emission.

An equilibrium reconstruction is necessary to map midplane measurements onto the detection planes and to compute path lengths through the plasma for inversion of line-integrated signals. The equilibrium code EFIT (Refs. 21 and 22) is used to map the poloidal flux surfaces when poloidal velocity inversions are performed. On NSTX, EFIT is typically run with constraints from the MPTS pressure profiles and the diamagnetic loop measurements, and includes currents in the vacuum vessel, but may also be constrained by MSE measurements of pitch angle, flux isotherms, and toroidal rotation.[23]

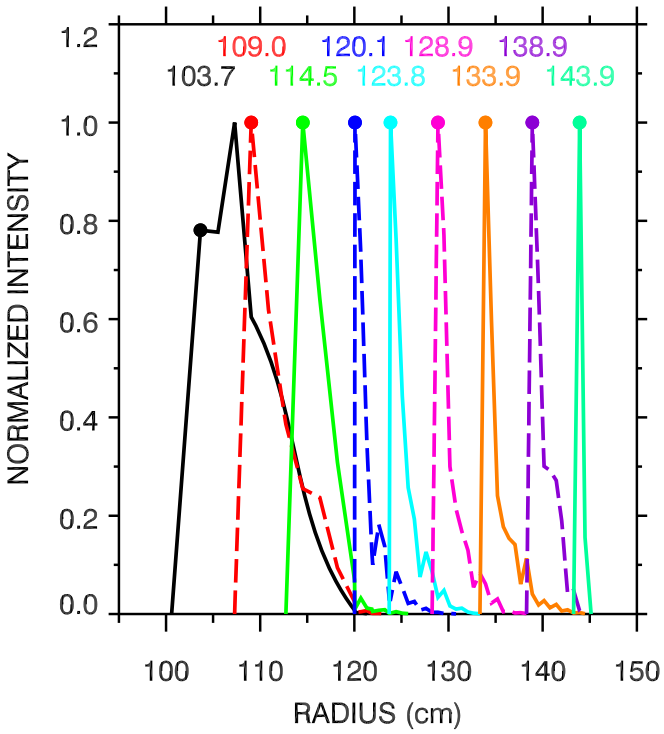

FIG. 3. (Color online) Normalized intensity along several sightlines shows radial smearing at various radii for shot 132484 at 0.596 s.

IV. MATRIX INVERSIONS

With the proper viewing location, a toroidal viewing array can achieve radial resolution on the order of a centimeter, since the width of a typical heating beam is much less than the major radius of the plasma. With vertical views, localization is more difficult, since the finite beam height must be compared to the plasma minor radius. When viewing closer to the magnetic axis, the finite height of the beam can cause considerable radial smearing, equivalent to the beam height divided by the local plasma elongation. Figure 3 shows one example of the radial smearing expected for a subset of the sightlines across the profile. Solid circles indicate the nominal radii of the sightlines. This smearing is directly computed using measured data and the method shown in Sec. IV B below.

Measurements taken in both the active and passive detection planes are line-integrated, so inversions to obtain local values of emissivity and velocity are necessary. A matrix inversion approach is used.[24] Subtraction of background emission (both intrinsic edge and plume emission) contributions requires inversion and remapping to the active viewing geometry.

A. Inversion of background emission

The background emissivity is assumed to be constant on a flux surface. The shape of the plasma is determined from an equilibrium reconstruction at each time. Emission zones are defined as regions near constant poloidal flux values. The measured brightness along each sightline (i) can be related to the emission in each zone (j) of the plasma by a length matrix L_{ij}.

$$4\pi B_i = \sum_j L_{ij} E_j, \tag{10}$$

where B_i is the measured brightness (in units of photons/s/cm^2/sr/s) and E_j is the local emissivity (in units of photons/s/cm^3/s) and the length matrix is determined from the path length of each sightline through each emissivity zone. The local emissivity can then be recovered from measured the brightness using a matrix multiplication of the inverted length matrix

$$E_j = 4\pi \sum_j L_{ji}^{-1} B_i. \tag{11}$$

The brightness weighted by the apparent line-integrated velocity ($B_i u_i$) can be related to the local velocity-weighted emissivity ($E_j v_j$)

$$4\pi B_i u_i = \sum_j L_{ij} E_j (\hat{s}_i \cdot \vec{v}_j) = \sum_j L_{ij} E_j v_j \cos\,\theta_{ij}, \tag{12}$$

where θ_{ij} are the angles between the sightlines and poloidal velocity directions. Defining a matrix, $M_{ij} \equiv L_{ij} \cos\,\theta_{ij}$, which adds the angular information to the length matrix, the local velocity for the background emission of C^{5+} ions can be obtained with two matrix inversions

$$v_j = \frac{E_j v_j}{E_j} = \frac{\Sigma_j M_{ji}^{-1} B_i u_i}{\Sigma_j L_{ji}^{-1} B_i}. \tag{13}$$

The calculation of the contribution of the background emission to the active views is accomplished by computing the velocity-weighted background emission. The inverted $E_j v_j$ for the background emission is determined and then interpolated onto the radial grid for the active emission. The velocity-weighted brightness contribution to the active view is then computed from a matrix multiplication of the matrix M_{ij} for the *active* view with the interpolated $E_j v_j$ from the *background* view

$$B_i^A u_i^A = \sum_j M_{ij}^A E_j^A v_j^A, \tag{14}$$

where u^A is the computed differential velocity, B^A is the background brightness for the active view, M_{ij}^A is the matrix for the active view, and $E^A v^A$ are the interpolated values for the sightlines in the active view based on the background measured values.

B. Inversion of active emission

The brightness weighted velocity due to CX emission is given by

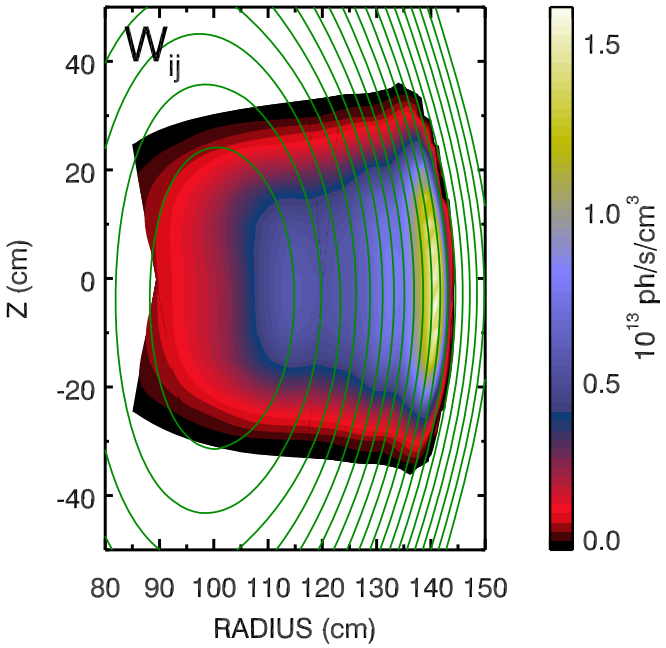

FIG. 4. (Color online) Contour plot of the weight matrix *Wij* for shot 132484 at 0.916 s overlaid with flux surface contours from EFIT.

$$B^{\mathrm{CX}} u^{\mathrm{CX}} = B^{\mathrm{TOT}} u^{\mathrm{TOT}} - B^{\mathrm{BKG}} u^{\mathrm{BKG}}, \tag{15}$$

where the $B^{\mathrm{TOT}} u^{\mathrm{TOT}}$ is the measured brightness weighted velocity from the active view, $B^{\mathrm{BKG}} u^{\mathrm{BKG}}$ is the brightness weighted velocity for the background contribution in the active view, which is computed with Eq. (14) using the measurements from the background view.

The CX emission is not constant on a flux surface, so inversion of the CX emission requires knowledge of *local* values of carbon density, beam neutral density, and CX rate along the sightlines [see Eq. (3)]. A nonorthogonal grid of emission zones and horizontal slices stacked in the vertical direction are used to compute a weight matrix, which is proportional to the CX emission

$$W_{ijk} = E_{ijk}^{\mathrm{CX}} = n_j^C n_{jk}^{\mathrm{beam}} \langle \sigma^{\mathrm{CX}} v \rangle_{ijk}^{\mathrm{eff}}, \tag{16}$$

where the subscript k refers to the vertical zones. Summing over vertical zones yields a two-dimensional (2D) weight matrix, W_{ij}. Values of such a weight matrix are shown as a contour plot in Fig. 4. A 2D carbon density profile is computed by mapping the local measurements from the toroidal CX system using the equilibrium contours. Likewise, the local T_e and n_e profiles, measured with Thomson scattering, are mapped onto 2D to provide input for a 2D beam attenuation calculation in the plane of measurement of the active view. Local values of T_i and v_ϕ are mapped into 2D to allow the calculation of local effective CX rates using computed rates from the Atomic Data and Analysis Structure (ADAS) database.[25] A length matrix L'_{ijk} is computed containing the local path lengths through this locally defined grid, now broken down to subpaths through the emission zones. Summing over the vertical zones returns the length matrix

$$L_{ij} = \sum_k L'_{ijk}. \tag{17}$$

The differential values of the apparent velocity-weighted brightness is related to local emissivity by

$$2\pi(B_i^{\mathrm{CX}} u_i^+ - B_i^{\mathrm{CX}} u_i^-) = \sum_{j,k} L'_{ijk} W_{ijk} \cos\,\theta_{ijk}, \tag{18}$$

where u_i^+ and u_i^- are apparent line-integrated velocities from upper and lower viewing sightlines, respectively. B_i^{CX} is the brightness due to the CX emission alone, which can be computed from local values mapped from midplane measurements

$$4\pi B_i^{\mathrm{CX}} = \sum_{j,k} L'_{ijk} W_{ijk}. \tag{19}$$

Two matrices are defined

$$P_{ij} \equiv \sum_k L'_{ijk} W_{ijk}, \tag{20}$$

$$Q_{ij} \equiv \sum_k L'_{ijk} W_{ijk} \cos\,\theta_{ijk}, \tag{21}$$

where P_{ij} relates to measured line-integrated brightness and Q_{ij} also contains the directional information of the projection along the sightlines. The differential velocity is then given by

$$u_i^{\mathrm{diff}} = \frac{1}{2}(u_i^{\mathrm{UP}} - u_i^{\mathrm{DOWN}}) = \sum_j Q_{ij} / \sum_j P_{ij}. \tag{22}$$

Using a single matrix inversion, the local poloidal velocity for the C^{6+} ions can be computed

$$v_j = \sum_j Q_{ji}^{-1} \left(u_i^{\mathrm{diff}} \sum_{j'} P_{ij'} \right). \tag{23}$$

Errors can be easily propagated through the matrix multiplications by recognizing that for a matrix multiplication of a vector x_i by matrix A_{ji}

$$y_j = \sum_j A_{ji} x_i \tag{24}$$

the variance of the result, y_j, is given by

$$\sigma_{y_j}^2 = \sum_i A_{ji}^2 \sigma_{x_i}^2. \tag{25}$$

V. POLOIDAL VELOCITY MEASUREMENTS

NSTX is a spherical torus with a major radius of 0.85 m, plasma current $I_p \leq 1.5$ MA, neutral beam power $P_{\mathrm{NB}} \leq 6$ MW, which operates with vacuum magnetic field $0.35\ \mathrm{T} \leq B_0 \leq 0.55$ T. Measured parameters for a typical lower-single-null (LSN) H-mode discharge with $B_0 = 0.45$ T, $I_p = 0.9$ MA, $P_{\mathrm{NB}} = 6$ MW, are shown in Fig. 5. A right-handed coordinate system is used. Positive toroidal direction is counterclockwise as seen from the top of the device; the direction of I_p is positive, opposite to the usual direction of the toroidal magnetic field. The poloidal magnetic field is positive and a positive poloidal velocity is downward at the outside midplane. The profile evolution of the T_e, T_i, n_e, n_c, and v_ϕ are shown in Fig. 6 at the early, middle, and late times indicated in Fig. 5. The measured profiles of line-integrated brightness and differential poloidal velocity u_{diff} at those same times are shown in Fig. 7. The total measured C^{5+} brightness from the active view, which includes both background and active CX emission, is plotted in the upper panels of Fig. 7 (black). The brightness profile for passive view is plotted in red. With three neutral beam sources, the active signal dominates the background signal at larger major radii, but is more comparable at smaller major radii due to the significant attenuation of the neutral beam density across the profile.

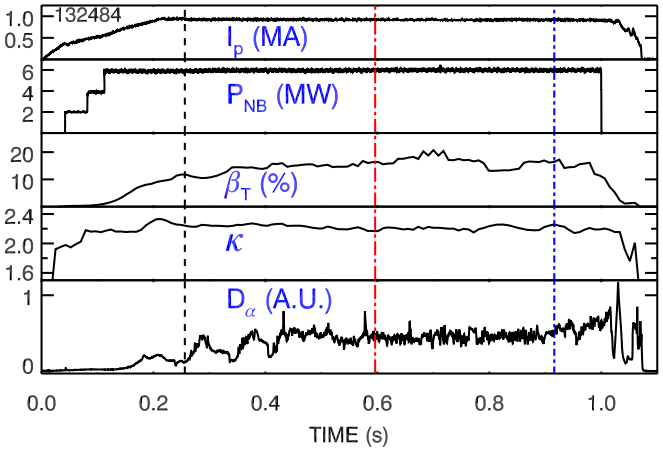

FIG. 5. (Color online) Discharge parameters for H-mode discharge 132484.

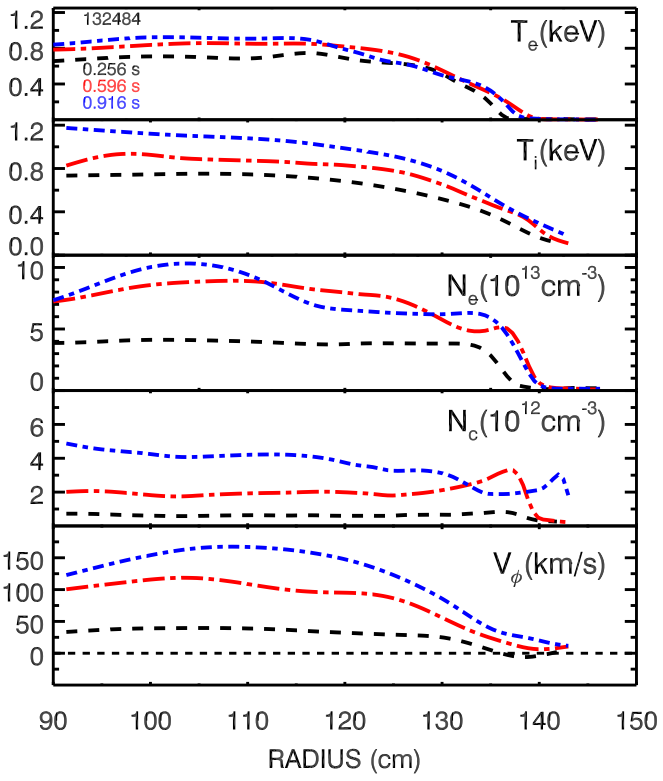

FIG. 6. (Color online) Measured plasma profiles at three times for shot 132484.

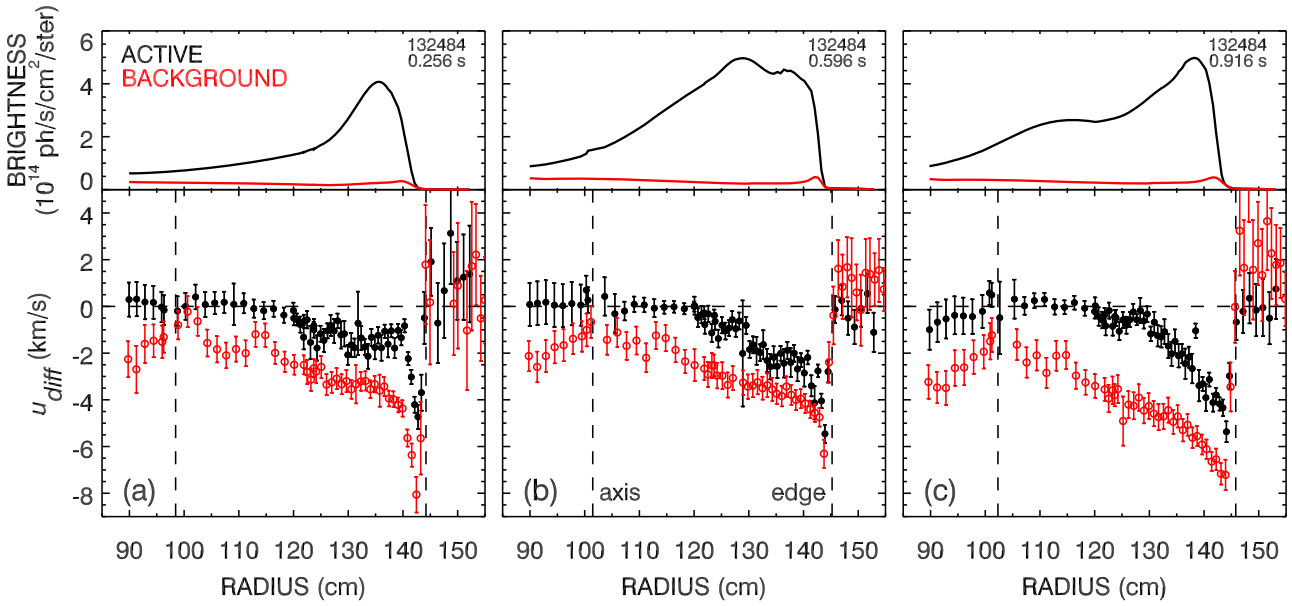

FIG. 7. (Color online) Brightness profiles of active and passive emission (upper panels) and line-integrated differential velocity profiles (lower panels) for active (black) and passive (red) views are shown at (a) 0.256 s, (b) 0.596 s, and (c) 0.916 s. The dashed vertical lines indicate the positions of the magnetic axis and plasma edge.

In the lower panels of Fig. 7, the solid black symbols show the measured differential velocities from up-down symmetric pairs of fibers. Two populations of C^{5+} ions contribute to these apparent velocities: the active CX emission represents the velocity of the parent C^{6+} ions in the beam volume, and the background emission represents the velocity of the intrinsic background and plume C^{5+} ions along the line of sight. The contribution from CX ions diminishes rapidly near the edge, due to reduced temperature, to the point where there is no C^{6+} population. The open red symbols in Fig. 7 show the line-integrated differential velocity of the background emission using the passive plane of measurement. Note the change in direction of u_{diff} at the plasma edge. A very tenuous population of C^{5+} ion is seen in the scrape off layer flowing in the ion diamagnetic direction, which has a positive sign for this discharge. Vertical dashed lines show the nominal positions of the magnetic axis and the plasma edge as computed from NSTX EFIT.

VI. COMPARISON TO NEOCLASSICAL THEORY

A. Local inverted velocity for H-mode plasma

The measured data are prepared for inversion by fitting with a smoothing spline.[26] The error of this nonparametric fit is determined by repeating the spline fit many times while randomly varying the values within a probability distribution whose width is equal to the measured errors. The smoothed spline values with their computed errors are then used in the matrix inversions.

The local poloidal velocity profile is determined as described in Sec. II B above using Eq. (23). The errors are propagated through this inversion process using Eq. (25). Inverted velocity profiles are plotted in Fig. 8 (black circles), which correspond to the line-integrated velocity profiles seen in Fig. 7. The radial extent of these profiles is confined to the radial region over which the CX emission is present. The poloidal velocity expected by NCLASS is overlaid (solid red

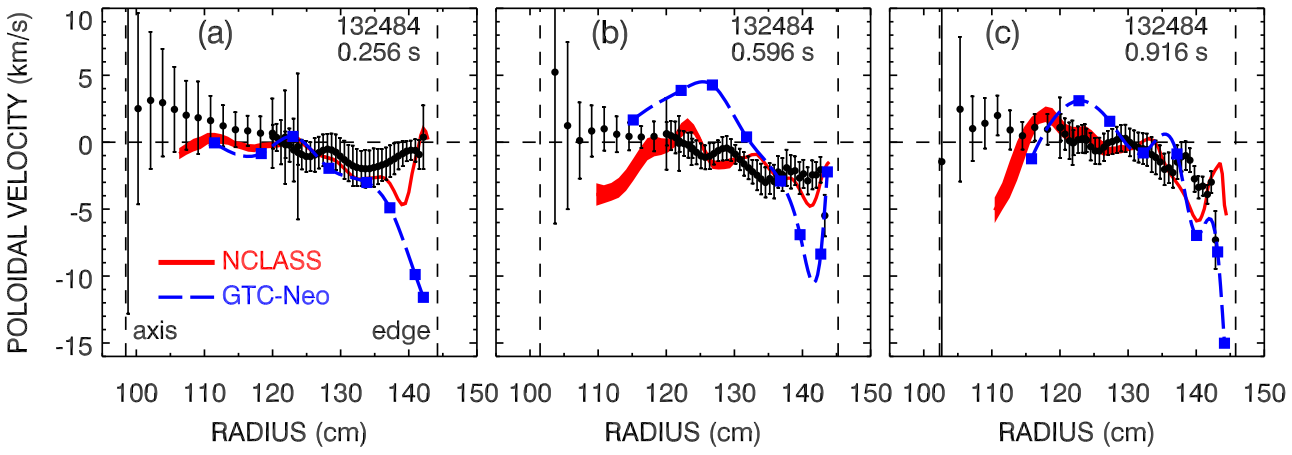

FIG. 8. (Color online) Inverted poloidal velocity (circles) overlaid with NCLASS (solid) and GTC-NEO (dashed) profiles at three times for shot 132484.

band) along with the GTC-NEO simulation (dashed blue). The GTC-NEO simulation is averaged over eight radial zones and the dashed line connecting them represents a spline fit. The vertical dashed lines indicate the plasma center and edge from NSTX EFIT. The uncertainties in the NCLASS poloidal velocity estimate due to experimental errors in the profiles of T_i, n_c, v_ϕ, and Z_{eff} are represented by the width of the band plotted in Fig. 8. A series of TRANSP runs were performed with inputted diagnostic profiles of T_i, n_c, v_ϕ, and Z_{eff} which have been randomly varied within a probability distribution represented by their error. The corresponding uncertainties for GTC-NEO profiles, though not computed, would be expected to be similar.

The measured poloidal values and the two neoclassical estimates show mixed agreement across the profile. There is better agreement between the measurements and the neoclassical estimates in the core plasma and worse near the edge, where the GTC-NEO code is known to be less accurate. At the earliest time, both NCLASS and GTC-NEO velocities deviate from the measured values outside of 135 cm. In this region, the neoclassical values deviate from each other. At the latest time, the NCLASS and GTC-NEO values seem to coincide but typically exceed the measured poloidal velocity in magnitude near the edge.

B. Reversed magnetic field

Neoclassical theory predicts that the direction of poloidal flow depends on the direction of the toroidal magnetic field.[27] Profiles for two similar discharges with opposite signs of toroidal magnetic field but equal magnitude are shown in Fig. 9. Shot 135686 is a LSN plasma with toroidal field in the usual direction for NSTX, i.e., opposite to the direction of the plasma current. Shot 135991 is an upper-single-null plasma with toroidal field in the reversed direction, parallel to the plasma current.

The local inverted impurity velocity profiles are plotted in Fig. 10 for the two discharges. The expected change in the direction of the measured carbon poloidal velocity for the reversed magnetic field case is shown in Fig. 10(a) compared to the normal direction shown in Fig. 10(b). The direction changes sign while the magnitude of the measured poloidal velocity is small in each case (<2 km/s), suggesting that any systematic error in the measured poloidal flow is quite small. The ion diamagnetic drift direction is in the negative direction for the reversed magnetic field case, [Fig. 10(a)] and in the positive direction for the usual magnetic field direction [Fig. 10(b)]. The neoclassical values for the two cases also show the change in direction of poloidal flow. As in the previous section, the measured and neoclassical values are similar in the core plasma, but differ significantly in the edge region. The neoclassical cases consistently predict larger magnitudes of the poloidal velocity than what is measured.

C. Magnetic field scan

Additional insight into the differences between measured poloidal velocity and neoclassical expectations is gained by examining the trends in poloidal velocity as plasma conditions are systematically varied. Neoclassical theory predicts that the magnitude of the poloidal velocity should scale inversely with the toroidal magnetic field. To test this, the toroidal magnetic field and plasma current were scanned over a series of well-matched discharges, while maintaining a constant I_p/B_0 ratio of 2.1 MA/T. The magnetic field was varied from 0.34 to 0.54 T as the plasma current was varied from 0.72 to 1.13 MA. Temperature, density, and velocity profiles at 0.416 s for these discharges are shown in Fig. 11. Measured poloidal velocity profiles showing a systematic variation are shown in Fig. 12(a). The expected neoclassical poloidal velocity profiles are shown for comparison in Figs. 12(b) and 12(c), for NCLASS and GTC-NEO, respectively. The neoclassical profiles seem to have much more radial structure than the measured profiles, especially nearer to the plasma edge. Some of this variation may be due to the uncertainty in the gradients of the measured diagnostic profiles. A mean poloidal velocity was computed over a radial range near the measured peak to eliminate some of this variation when considering dependence on magnetic field. This region is indicated in Fig. 12 as a shaded band covering the range between 137 and 141 cm. The mean poloidal velocity is plotted in Fig. 13 as a function of magnetic field amplitude and its reciprocal. The solid lines indicate a linear fit to the mean poloidal-velocity data. The measured mean poloidal velocity (circles) shows the expected trend with magnetic field, scaling linearly with $1/B_0$, even though measured values change only 1.5 km/s. The NCLASS values (triangles) and the GTC-NEO values (squares) also show an increase in the magnitude of the poloidal velocity as the magnetic field is reduced.

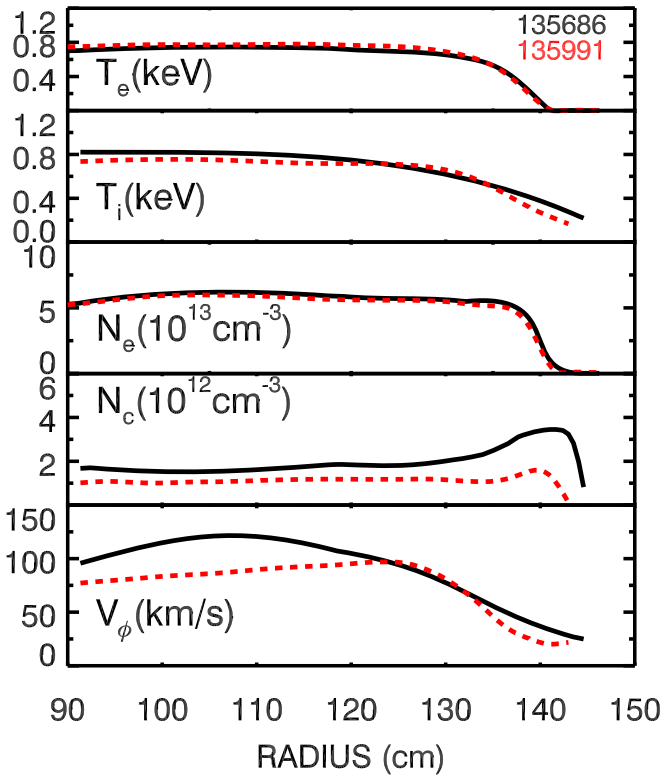

FIG. 9. (Color online) Plasma profiles for shot 135686 with $B_\phi<0$ (solid) and shot 135991 with $B_\phi>0$ (dashed).

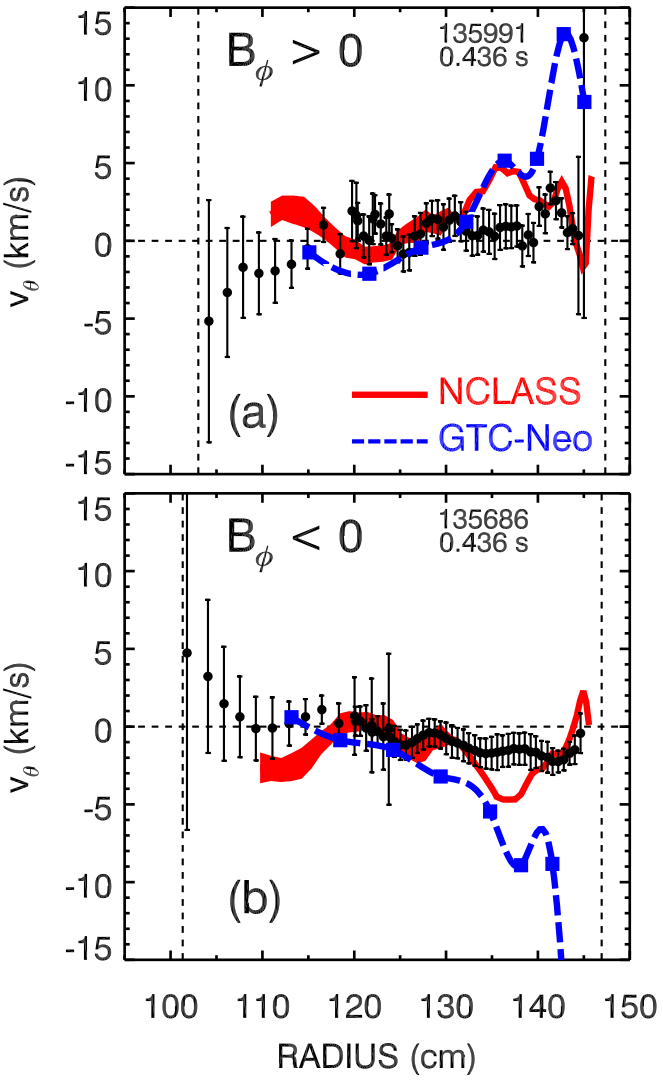

FIG. 10. (Color online) Measured local poloidal velocity overlaid with NCLASS and GTC-NEO profiles for (a) reversed magnetic field, $B_\phi > 0$ and (b) "normal" magnetic field, $B_\phi < 0$.

Much larger poloidal flow than what is measured is expected from the neoclassical simulations, especially at lower magnetic field. The neoclassical codes NCLASS and GTC-NEO both expect a more rapid change in poloidal velocity with magnetic field than what is actually measured. At this radial location, the fitted slope for the NCLASS data is 2.6 times the fitted slope for the measured data. The slope for the GTC-NEO data is 3.3 times the fitted slope of the measured data.

D. Radial electric field

The radial electric field can now be determined since all of the components of the radial force balance equation [Eq. (1)] have been measured. The individual components of E_r are plotted in Fig. 14(a). The contribution of the poloidal velocity term $-v_\theta B_\phi$ is quite small compared to the large contribution from the toroidal velocity term $v_\phi B_\theta$, which typically dominates the other terms. In a spherical torus with $B_\phi/B_\theta \sim 1$, the value of the poloidal velocity does not have as much leverage in the force balance equation as it would in a conventional tokamak where $B_\phi/B_\theta \sim 10$. The measured E_r profile does not extend all the way to the plasma edge, since the C^{6+} ion is not present at the cooler edge temperatures on NSTX. Figure 14(b) overlays the measured E_r profile with the NCLASS and GTC-NEO expectations of E_r. In this case, the toroidal impurity velocity profile is used as an input to both neoclassical codes, so the apparent agreement between the E_r profiles simply reflects that the differences between the measured and neoclassically expected poloidal velocity values are small compared to the magnitude of E_r. The external module for NCLASS was required for this calculation, since the module in TRANSP did not self-consistently handle the E_r. Both neoclassical codes suggest that large gradients in E_r might exist near the plasma edge beyond the region in which CX measurements are available.

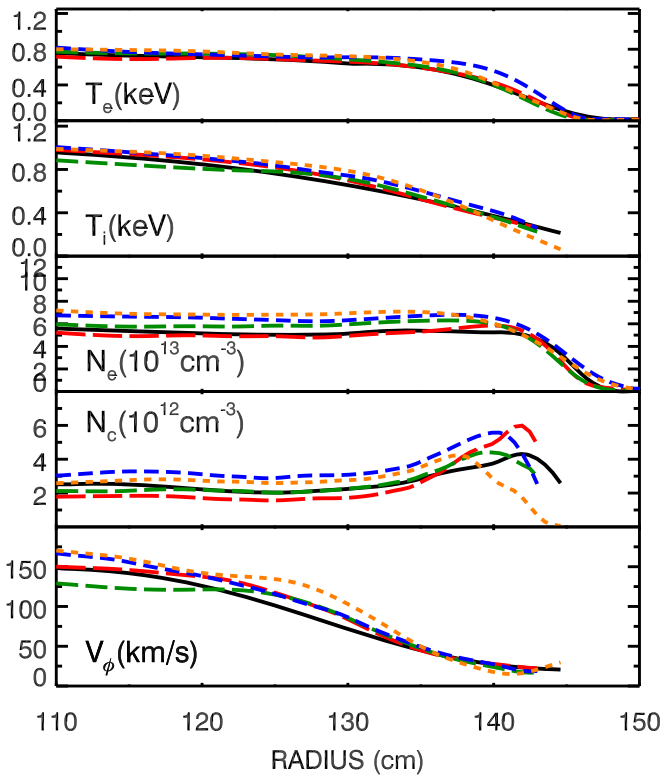

FIG. 11. (Color online) Plasma profiles for discharges from scan of B_ϕ and I_p.

VII. DISCUSSION

CX recombination spectroscopy can be used to measure all the components in the force balance equation in order to obtain E_r. Great care must be exercised when making poloidal velocity measurements using this technique. The energy-dependent CX cross section causes an additional apparent velocity that is directed against the flow of the neutral beam particles. With sufficient magnetic field and temperature the gyromotion of the impurity ion can lead to additional vertical components in the apparent velocity. Uncertainties in the CX cross section may lead to systematic errors that could be comparable to or greater than the poloidal velocity itself. Measurements uncorrected for the atomic physics or incompletely corrected will show that poloidal velocity will scale with ion temperature and magnetic field.

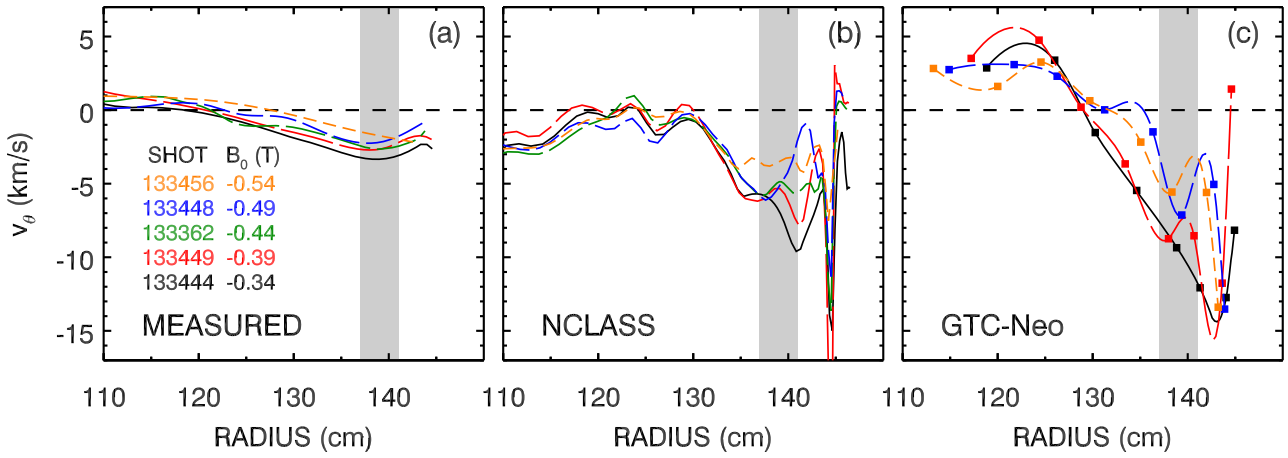

FIG. 12. (Color online) Poloidal velocity profiles for B_0 and I_p scan showing (a) measured, (b) NCLASS, and (c) GTC-NEO values of poloidal velocity.

Poloidal velocity measurements on NSTX take advantage of the plasma symmetry with respect to the midplane and the horizontal direction of neutral beam injection to eliminate the dependence on the complicated atomic physics corrections for line-integrated poloidal velocity measurements. The only use of atomic physics is to compute a relative CX emission along the viewing chord for an inversion to obtain local poloidal velocity. The computation of CX emission is much less sensitive to the uncertainties in the magnitude and shape of the CX cross sections. The low magnetic field and modest temperatures of NSTX eliminate the worry of the contributions from gyro orbit finite lifetime effects.

The measured poloidal velocity on NSTX behaves qualitatively as expected from neoclassical theory, scaling inversely with toroidal magnetic field and reversing direction when the direction of the toroidal magnetic field is reversed.

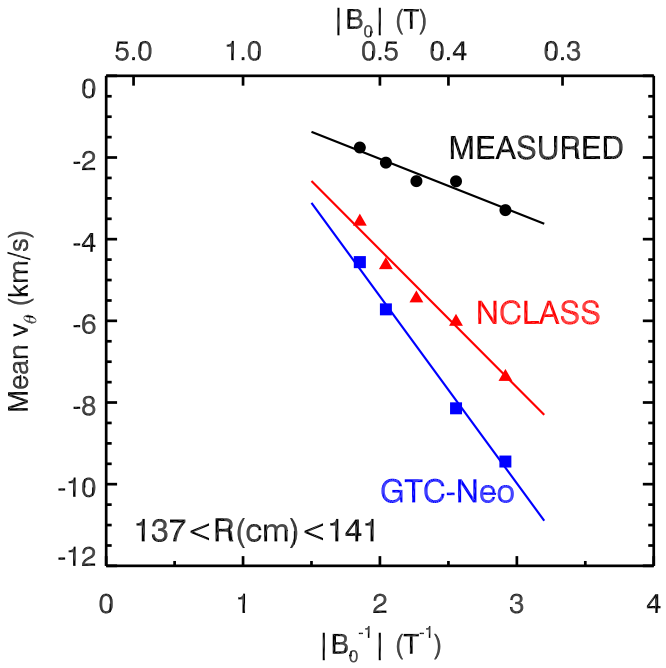

FIG. 13. (Color online) Mean poloidal velocity for 137 cm$<R<$141 cm plotted vs $|B_0|^{-1}$ for measured, NCLASS, and GTC-NEO values.

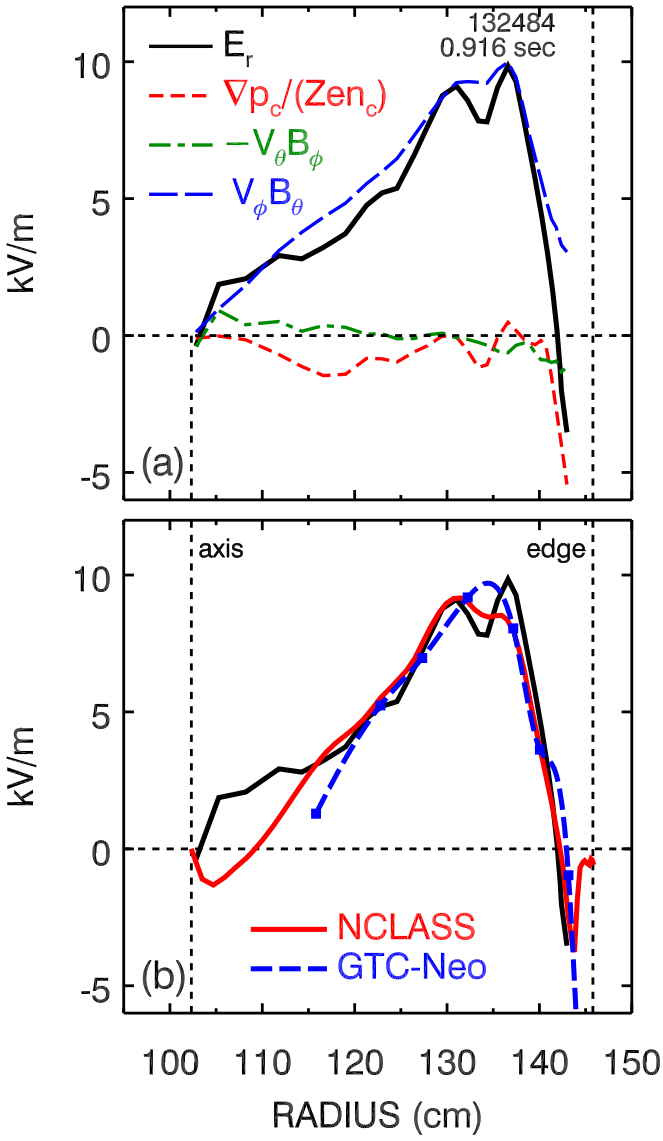

FIG. 14. (Color online) (a) Measured components of E_r in the radial force balance equation for shot 132484 at 0.916 s. The contribution from the poloidal velocity component is small compared to the other terms. (b) Comparison of measured E_r with that inferred from NCLASS and GTC-NEO.

The low magnitudes of the poloidal velocity for the pair of discharges with opposite magnetic field direction suggest that any systematic errors are small. These behaviors give some confidence in the veracity of the poloidal velocity measurements. The measured poloidal velocity profiles on NSTX are equal to or lower in magnitude than expected from neoclassical calculations from NCLASS and GTC-NEO, in contrast to measurements on JET and DIII-D.[2–4] Differential changes in measured mean poloidal velocity are seen to be a factor of 2.6–3.3 lower than changes in NCLASS and GTC-NEO. There is no indication of an inconsistency with the direction of the measured poloidal velocity compared to neoclassical expectations, as was observed on DIII-D.[4] These results are consistent with measurements on MAST, which showed that, within experimental error, the measured poloidal flow was similar to neoclassical values in magnitude and direction.[6] Due to the relatively low values of measured poloidal velocity, the difference between measured E_r and that computed from neoclassical is quite small.

ACKNOWLEDGMENTS

This work was supported by the U.S. Department of Energy under Contract No. DE-AC02-09CH11466.

[1] F. M. Levinton, R. E. Bell, S. H. Batha, E. J. Synakowski, and M. C. Zarnstorff, Phys. Rev. Lett. **80**, 4887 (1998).
[2] K. Crombé, Y. Andrew, M. Brix, C. Giroud, S. Hacquin, N. C. Hawkes, A. Murai, M. F. F. Nave, J. Onegana, V. Parail, G. Van Oost, I. Voitsekhovitch, and K.-D. Zastrow, Phys. Rev. Lett. **95**, 155003 (2005).
[3] T. Tala, Y. Andrew, K. Crombé, P.C. de Vries, X. Garbet, N. Hawkes, H. Nordman, K. Rantamäaki, P. Strand, A. Thyagaraja, J. Weiland, E. Asp, Y. Baranov, C. Challis, G. Corrigan, A. Eriksson, C. Giroud, M.-D. Hua, I. Jenkins, H.C.M. Knoops, X. Litaudon, P. Mantica, V. Naulin, V. Parail, K.-D. Zastrow, and JET-EFDA contributors, Nucl. Fusion **47**, 1012 (2007).
[4] W. M. Solomon, K. H. Burrell, R. Andre, L. R. Baylor, R. Budny, P. Gohil, J. Groebner, C. T. Holcomb, W. A. Houlberg, and M. R. Wade, Phys. Plasmas **13**, 056116 (2006).
[5] B. J. Ding, Y. Sakamoto, and Y. Miura, Plasma Phys. Controlled Fusion **47**, 789 (2005); Chin. Phys. **16**, 3434 (2007).
[6] A. R. Field, J. McCone, N. J. Conway, M. Dunstan, S. Newton, and M. Wisse, Plasma Phys. Controlled Fusion **51**, 105002 (2009).
[7] S. M. Kaye, M. G. Bell, R. E. Bell, J. Bialek, T. Bigelow, M. Bitter, P. Bonoli, D. Darrow, P. Efthimion, J. Ferron, E. Fredrickson, D. Gates, L. Grisham, J. Hosea, D. Johnson, R. Kaita, S. Kubota, H. Kugel, B. LeBlanc, R. Maingi, J. Manickam, T. K. Mau, R. J. Maqueda, E. Mazzucato, J. Menard, D. Mueller, B. Nelson, N. Nishino, M. Ono, F. Paoletti, S. Paul, Y-K. M. Peng, C. K. Phillips, R. Raman, P. Ryan, S. A. Sabbagh, M. Schaffer, C. H. Skinner, D. Stutman, D. Swain, E. Synakowski, Y. Takase, J. Wilgen, J. R. Wilson, W. Zhu, S. Zweben, A. Bers, M. Carter, B. Deng, C. Domier, E. Doyle, M. Finkenthal, K. Hill, T. Jarboe, S. Jardin, H. Ji, L. Lao, K. C. Lee, N. Luhmann, R. Majeski, S. Medley, H. Park, T. Peebles, R. I. Pinsker, G. Porter, A. Ram, M. Rensink, T. Rognlien, D. Stotler, B. Stratton, G. Taylor, W. Wampler, G. A. Wurden, X. Q. Xu, L. Zeng, and NSTX Team, Phys. Plasmas **8**, 1977 (2001).
[8] R. E. Bell and E. J. Synakowski, AIP Conf. Proc. **547**, 39 (2000).
[9] W. A. Houlberg, K. C. Shaing, S. P. Hirshman, and M. C. Zarnstorff, Phys. Plasmas **4**, 3230 (1997).
[10] W. X. Wang, G. Rewoldt, W. M. Tang, F. L. Hinton, J. Manickam, L. E. Zakharov, R. B. White, and S. Kaye, Phys. Plasmas **13**, 082501 (2006).
[11] R. J. Hawryluk, in *Physics of Plasmas Close to Thermonuclear Conditions*, edited by B. Coppi, G. G. Leotta, D. Pfirsch, R. Pozzoli, and E. Sindoni (CEC/Pergamon, Brussels, 1980), Vol. 1, p. 19.
[12] R. A. Kolesnikov, W. X. Wang, F. L. Hinton, G. Rewoldt, and W. M. Tang, Phys. Plasmas **17**, 022506 (2010).
[13] P. E. Ciddor, Appl. Opt. **35**, 1566 (1996).
[14] J. D. Garcia and J. E. Mack, J. Opt. Soc. Am. **55**, 654 (1965).
[15] A. Blom and C. Jupén, Plasma Phys. Controlled Fusion **44**, 1229 (2002).
[16] M. von Hellermann, P. Breger, J. Frieling, R. König, W. Mandl, A. Maas, and H. P. Summers, Plasma Phys. Controlled Fusion **37**, 71 (1995).
[17] R. K. Janev, R. A. Phaneuf, H. Tawara, and T. Shirai, At. Data Nucl. Data Tables **55**, 201 (1993).
[18] R. J. Fonck, D. S. Darrow, and K. P. Jaehnig, Phys. Rev. A **29**, 3288 (1984).
[19] R. E. Bell, Rev. Sci. Instrum. **77**, 10E902 (2006).
[20] R. E. Bell, L. E. Dudek, B. Grek, D. W. Johnson, and R. W. Palladino, Rev. Sci. Instrum. **70**, 821 (1999).
[21] L. L. Lao, R. D. Stambaugh, A. G. Kellman, and W. Pfeiffer, Nucl. Fusion **25**, 1611 (1985).
[22] S. A. Sabbagh, S. M. Kaye, J. E. Menard, F. Paoletti, M. Bell, R. E. Bell, J. M. Bialek, M. Bitter, E. D. Fredrickson, D. A. Gates, A. H. Glasser, H. Kugel, L. L. Lao, B. P. LeBlanc, R. Maingi, R. J. Maqueda, E. Mazzucato, D. Mueller, M. Ono, S. F. Paul, M. Peng, C. H. Skinner, D. Stutman, G. A. Wurden, W. Zhu, and NSTX Research Team, Nucl. Fusion **41**, 1601 (2001).
[23] S. A. Sabbagh, A. C. Sontag, J. M. Bialek, D. A. Gates, A. H. Glasser, J. E. Menard, W. Zhu, M. G. Bell, R. E. Bell, A. Bondeson, C. E. Bush, J. D. Callen, M. S. Chu, C. C. Hegna, S. M. Kaye, L. L. Lao, B. P. LeBlanc, Y. Q. Liu, R. Maingi, D. Mueller, K. C. Shaing, D. Stutman, K. Tritz, and C. Zhang, Nucl. Fusion **46**, 635 (2006).
[24] R. E. Bell, Rev. Sci. Instrum. **68**, 1273 (1997).
[25] H. P. Summers, "Atomic data and analysis structure," JET Report No. JET-IR(94)-06 (1994).
[26] C. H. Reinsch, Numer. Math. **10**, 177 (1967); **16**, 451 (1971).
[27] Y. B. Kim, P. H. Diamond, and R. J. Groebner, Phys. Fluids B **3**, 2050 (1991).